Advanced Functional Materials

ADVANCED FUNCTIONAL MATERIALS
www.afm-journal.de

RESEARCH ARTICLE

Single-Signal Acoustic Imaging by AI-Assisted Synthesized Frequency Codec Beyond Limitation of Spatial and Temporal Dimensions

Wei Wang[1] | Jie Hu[2] | Bin Li[1,3] | Jingjing Liu[1] | Yang Tan[1] | Chengyu Zhao[1] | Rong Wang[1] | Jing Yang[1] | Bin Liang[1,4] | Johan Christensen[5] | Jian-Chun Cheng[1]

[1]Key Laboratory of Modern Acoustics, MOE, Institute of Acoustics, Department of Physics, Collaborative Innovation Center of Advanced Microstructures, Nanjing University, Nanjing, P. R. China | [2]Department of Information Science and Technology, Nanjing Forest University, Nanjing, P. R. China | [3]School of Mechanical Engineering, Wuhan Polytechnic University, Wuhan, P. R. China | [4]Jiangsu Physical Science Research Center, Nanjing, P. R. China | [5]IMDEA Materials Institute, Getafe, Madrid, Spain

Correspondence: Jingjing Liu (liujingjing@nju.edu.cn) | Bin Liang (liangbin@nju.edu.cn) | Johan Christensen (johan.christensen@imdea.es) | Jian-Chun Cheng (jccheng@nju.edu.cn)

Received: 10 March 2026 | **Revised:** 8 May 2026 | **Accepted:** 21 May 2026

Keywords: disordered medium | neural network | single-signal acoustic imaging | synthesized frequency codec

ABSTRACT

Acoustic images have been widely used across diverse disciplines, ranging from medical to industry to military applications. Existing mechanisms always require multiple signals, which are either single-measured by a complicated phased array in real-time or multiple-measured by a single sensor with a time delay. To overcome the long-standing contradiction between the spatial and temporal dimensions in imaging systems, here we propose a mechanism that enables acoustic imaging from a single signal, based on a synthesized frequency codec achieved through the combination of artificial material and artificial intelligence (AI). The artificial material, with its inherent randomness and dispersion, mimics multiple masks in the spectral domain to produce scattered waves at synthesized frequencies. These waves, as analytically proven, carry sufficient geometric information about the object to enable complete acoustic imaging. Such spectral fingerprints are then decoded in real-time by the AI, with no prior knowledge of material parameters. Thanks to this symbiosis, we demonstrate experimentally high-precision reconstruction of complex objects based on a single signal captured by a single fixed sensor, which breaks the limitations in both spatial and temporal dimension simultaneously. Our mechanism may revolutionize the imaging techniques for various scenarios, such as medical diagnosis, and beyond.

1 | Introduction

Because of the unique advantages in terms of radiation exposure, penetration depth, cost-effectiveness and biocompatibility, acoustic imaging plays an extremely important role in many fields such as medical diagnosis, industrial non-destructive testing, and underwater target detection [1–11]. To reconstruct the complex geometries for various objects like material failure, submarines, and human organs, signals captured by the sensors must contain enough information about the target objects. Conventional acoustic imaging techniques usually utilize sophisticated phased arrays with a bulky size to quickly obtain the spatial information

Wei Wang and Jie Hu contributed equally to this work.

of objects [3, 12–16], whose system complexity and size necessitates that the imaging systems cover a broader spatial dimension. In comparison, other kinds of imaging methods, whether traditional or compressed-sensing-based, use one sensor to receive necessary signals multiple times with dynamic spatial scanning [17] or multi-mode mask switching [18–21], which offers simplicity and compactness in spatial dimension, but gives rise to time delays and makes real-time imaging cumbersome to attain. Despite the wide application of deep learning in the field of imaging to facilitate data processing, existing imaging schemes still depend on information distributed at different points in either spatial or temporal dimensions [22, 23], directly resulting in the persistent conflict among these two dimensions of imaging in acoustics and related realms. In this context, a fundamental question naturally arises: Is it necessary for imaging information to be carried by multiple signals?

To answer this fundamental question, we revisit the essence of imaging and explore the possibility of realizing acoustic imaging based on a single signal. To get sufficient information from an image through its scattered field, conventionally, either a single measurement with multiple sensors in real time or multiple measurements by a single sensor involving time delay are conducted. In contrast, we propose a mechanism to convert the information of the scattered field from the high-dimensional spatial-temporal domain to the dimension-reduced frequency domain by marrying an artificial material [24–29] with artificial intelligence (AI) [30–33], which features fast imaging speed, low-cost fabrication, compact system size, and high imaging quality. Here, we choose to image the objects based on a single signal with a synthesized frequency by a disordered medium, which for the first time enables reducing the system's dimension in both space and time simultaneously. We verify that a disordered medium [34–39], which is commonly considered detrimental to imaging due to wave scattering of uncontrollable complexity, can counterintuitively be used to reduce the imaging system's dimension by combining it with AI technology. Due to the rich complexity arising from the medium's random parameter distribution and strong dispersion characteristics, it can serve as a series of masks with distinct parameter distributions at different frequencies, which enables synthesized frequency encoding from the spatial distribution of the whole scattered field to the frequency spectrum of a signal received once at a single point. Hence, every frequency component of the signal contains different information about the imaged objects. By harnessing the remarkable learning and feature-extraction abilities of neural networks [40], on the other hand, such an encoded single signal can be utilized to quickly integrate the information carried by the different frequency components and then reconstruct the geometry of the original object, without the need of prior knowledge of the material parameters. Hence, the medium used in our experiment, which was handcrafted at a cost much less than one dollar, proved sufficient to yield high imaging quality. Our proposed imaging mechanism with the coalescence of a disordered medium and AI may significantly reduce the cost of acoustic imaging while keeping the fast speed in the future.

2 | Results

2.1 | Mechanism of Single-Signal Acoustic Imaging by AI-Assisted Synthesized Frequency

In previous imaging methods, the contradiction between the spatial and temporal dimensions mainly results from the fact that the necessary information for imaging is distributed among various signals. This directly leads to significant challenges in achieving dimensionality reduction in the system, because the reduction of one dimension inevitably gives rise to the increase of the other dimension, making real-time imaging and single-sensor imaging cannot be realized simultaneously. To overcome this challenge, we propose an acoustic imaging mechanism based on only one single signal with an AI-assisted synthesized frequency codec. As shown in Figure 1a, a single fixed source emits a single signal chosen as a short pulse with a broadband spectrum, which undergoes scattering after insonifying an object of arbitrary shape. The scattered ultrasound field carrying the object's geometry information interacts with the disordered medium with randomness and dispersion, which can further be effectively captured via a single fixed sensor behind the medium. Then the received signal, encoded with the object's information, can be decoded to reconstruct the object's image by a neural network that holds the ability of information extraction. Note that the signal used for imaging is measured one single time at a single location and decoded in real-time for calculation, thus our mechanism can realize the maximized reduction in both the spatial and temporal dimensions (see Figure 1b).

To realize synthesized frequency encoding, here the disordered medium is introduced to provide distinct amplitude and phase distribution at different frequencies (Figure 1c), expressed as $M(x, y; \omega)$, where (x, y) is the spatial coordinate, and ω is the circular frequency. Thus, the disordered medium can modulate the spatial patterns of scattered waves of objects in distinct ways at different frequencies. It is worth noting that the multipath effects and time delays introduced by the scattering medium can be regarded as modulations of the phase and amplitude of the acoustic field, and are therefore already incorporated into the M. When the scattered waves arrive at the medium, the acoustic pressure distribution can be expressed as $p_{\mathrm{inc}}(x, y; \omega)$. Then, after the modulation of the disordered medium and propagating a distance l, the pressure received by a single sensor can be obtained by applying the Helmholtz–Kirchhoff equation, as follows [Correction added on June 16, 2026, after first online publication: Equation (1) has been amended in this version.]

$$p_{\mathrm{rec}}(\omega) = \iint_S \frac{e^{-\frac{i\omega r}{c}}}{2\pi r}\left(\frac{i\omega}{c} + \frac{1}{r}\right)\frac{l}{r} p_{\mathrm{inc}}(x, y; \omega) \cdot M(x, y; \omega)\, dxdy \tag{1}$$

where $\cdot$ denotes a point-wise multiplication, $r = \sqrt{(x - x_{\mathrm{rec}})^2 + (y - y_{\mathrm{rec}})^2}$, and $(x_{\mathrm{rec}}, y_{\mathrm{rec}})$ is the location of the received point. Equation (1) shows that the spatial distribution of the object's scattered wave can be effectively encoded into the frequency spectrum of a single signal received at a single point within the medium with dispersion and

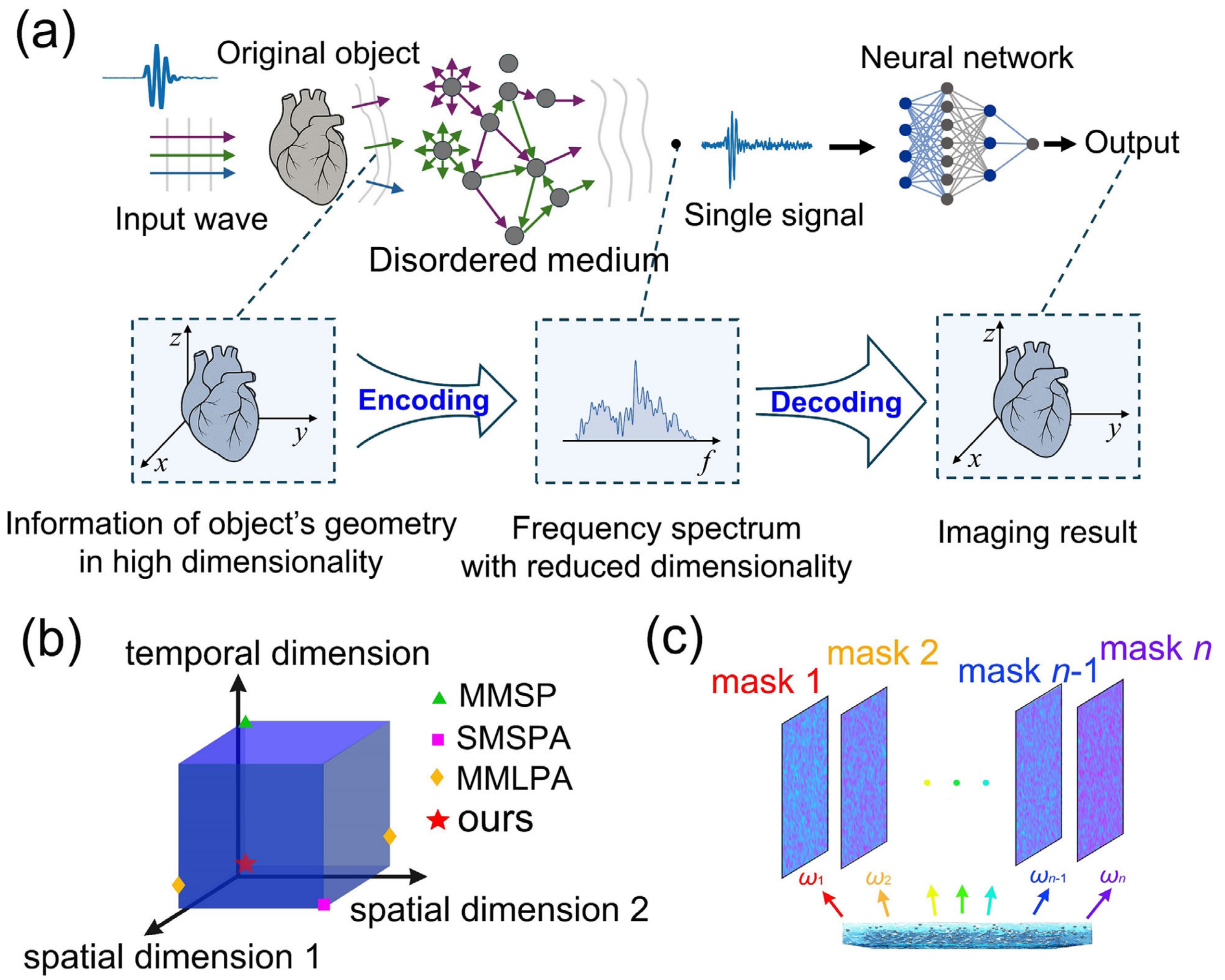

FIGURE 1 | Mechanism of single-signal acoustic imaging by AI-assisted synthesized frequency codec. (a) Schematic of the proposed mechanism. (b) Dimensionality reduction by our proposed mechanism compared with other current technologies. The different signs represent different technologies (MMSP: multi-measurement with single probe, SMSPA: single-measurement with spatial probe array, MMLPA: multi-measurement with linear probe array, ours: our proposed mechanism of single-signal acoustic imaging by AI-assisted synthesized frequency). The distance between signs and the origin of the coordinate means the dimension occupied by the corresponding imaging system. (c) Encoding mechanism of the disordered medium. The disordered medium serves as different masks at different frequencies.

randomness. More specifically, the dispersion ensures the masks are distinct at different frequencies, making the modulation of the incident wave in different ways, while the randomness enables the remarkable enhancement of such differences and further guarantees the information required for imaging is fully encoded in the spectrum. Thus, the amplitude in different frequencies can carry different information about the acoustic field. By contrast, without a disordered medium, the responses at different frequencies are highly correlated (see Figure S1), leading to significant information redundancy and preventing effective imaging, which is discussed in detail in Section S1. This indicates that the imaging of the object can be realized based on suitable decoding methods. Here, instead of analytically retrieving the scattered waves under the premise of known $M(x, y; \omega)$, we choose to use a neural network to directly connect the received signal and the object's image by extracting the information synthesized in the frequency spectra. This can significantly increase the imaging speed and does not need any prior knowledge of the disordered medium, which is totally different from the compressed-sensing-based methods [18, 41] and significantly enhances the practicality of the proposed mechanism in real-world scenarios. Thus, any medium with random parameter distribution and high dispersion can be used for imaging, which significantly reduces the cost of fabrication. The robustness of our mechanism is primarily determined by the disordered medium, whose intrinsic randomness makes the system sensitive to external perturbations. In practice, such perturbations can be incorporated into the training process, enabling the model to learn robust representations and maintain stable performance.

2.2 | Fabrication and Characterization of the Disordered Medium

To verify that the medium used in our system does not require any judicious design and parameter retrieving but instead relies solely on dispersion and randomness, we choose to handmake the sample rather than using sophisticated precision machining processes. The medium consists of an agar slab encapsulating randomly distributed steel beads, as shown in Figure 2a. Initially, an agar solution is subject to controlled heating until it reaches its boiling point, followed by a subsequent increase in temperature until a viscous state is attained. Next, a certain amount of steel beads is blended into the solution, after which a cooling process is initiated, solidifying the material. Devoid of costly precision fabrication and advanced measurement instruments during this process, our medium solely requires facile random blending of steel beads. The diameter of the beads is chosen as corresponding to the wavelength of the operating frequency band to support sufficient multiple scattering, providing the medium with adequate dispersion characteristics. Detailed fabrication procedures and material recipes are provided in Section S2. To verify the randomness of the medium, we conducted an experiment where the medium was impinged by sinusoidal pulses with a center frequency of 2.5 MHz and a cycle number of 2, which is discussed in detail in Sections S3 and S4.

Measurements were taken at five points (green dots in Figure 2b) at the back of the medium to analyze the transmitted signals in an underwater setup, see Figure 2c. To exclude the contributions other than the direct-path wave and its coda, a time window was applied around the direct-path segment. Since the signal acquired in our system contains both the direct wave and the coda wave (as depicted in Figure 2d), the total acquisition time window is chosen to be longer than the duration of the emitted signal. Although the disordered medium, the transducer, and imaging object appear spatially close in the schematic, their actual separation is at least on the order of several tens of wavelengths. Therefore, reflections from these components arrive at sufficiently different times and can be readily separated from the direct-path signal in the time domain. The temporal and frequency domain distributions of the received signals are shown in Figure 2d,e, respectively, which clearly display strong disparity and indicate pronounced randomness. This guarantees efficient information encoding during the imaging process, which is a necessary prerequisite for successful imaging. In addition, the resolution of our mechanism is fundamentally determined by the diffraction limit, as in conventional ultrasound imaging methods. Nevertheless, for conventional ultrasound imaging, approaching this diffraction-limited resolution typically requires a large-aperture transducer to generate sufficiently fine focal spots for scanning-based imaging. In contrast, our approach does not rely on focusing or scanning. Instead, it utilizes the disordered medium to map the diffraction field over the entire spatial cross-section into the spectral response measured by a single sensor.

2.3 | Experimental Realization of Single-Signal Acoustic Imaging

After completing the medium fabrication and randomness characterization, we conduct the imaging experiments in an underwater ultrasonic system, with possible relevance to non-destructive testing, medical diagnostics, and underwater detection. To validate the effectiveness of our mechanism across objects with different impedance distributions without losing generality, we choose to image a variety of handwritten digits from the known Mixed National Institute of Standards and Technology (MNIST) database [42]. 700 handwritten digits from the MNIST Database are selected and engraved in metal plates as the objects to be imaged, with 70 samples for each digit from 0 to 9 (see Figures S2 and S3), which is discussed in detail in Sections S5 and S6. As Figure 2c shows, submerged in a water container, an ultrasonic transducer emits the same broadband signal as that in randomness characterization, which passes through the object and disordered medium in succession and is received by a single fixed probe located behind the medium. The detailed experimental setup is provided in Section S7 and Figure S4.

We sequentially measured and recorded the signals, among which 600 samples were allocated for the training set, while 100 samples were designated for the test set, as shown in Figure 3a. Figure 3b–k, presents the normalized spectra of the signals received by the probe corresponding to ten handwritten digits (0–9) at the top left corner. Although these spectra appear highly intricate and it is hard to extract the shape information of the digits by traditional methods, the spectra indeed exhibit certain variations but also some level of shape-similarity in relation to comparable handwritten digits, for example, 4 and 9, as well as 5 and 6. This indicates that different energy distributions in spectra can reflect the shape information of different digits and thus the spectra can be considered as a kind of frequency-dependent "fingerprint", which is the precondition of our imaging method. This signal acts as the input dataset for training the neural network, while the labels for the neural network are the shapes of the objects. We employ a simple multilayer perceptron with two hidden layers, which are proven to be highly effective in imaging scattered objects such as handwritten digits (the detailed training process is discussed in Section S8).

The detailed imaging results are shown in Figures 4 and 5. Here, we use the structural similarity (SSIM) between original objects and imaging results to evaluate the imaging quality. Through a simple neural network, the average SSIM for the training and test sets can reach 0.9870 and 0.7853, respectively. We select typical imaging results for 10 handwritten digits from the training and test sets, as shown in Figure 4. Figure 4a,b compares the original shapes of the objects and the corresponding imaging results for the training set, respectively. And Figure 4e–j presents the comparison of original objects and some typical imaging results in Figure 4a,b in terms of image profiles along the particular horizontal and vertical directions. The differences between these two sets of images are close to negligible in both images and one-dimensional profiles, thereby implying a near-complete reconstruction of the shape information. Similarly, Figure 4c–p are some typical results for the test set and their original references, wherein the comparison also demonstrates a remarkable degree of resemblance, showcasing the high fidelity and accuracy of the imaging process. Therefore, it can be concluded that our mechanism can encode efficient information from the spatial to frequency dimension and realize the imaging by a neural network based on one single signal encoded with sufficient information. It is also worth mentioning that, once the neural network has been trained, the entire imaging process can be completed within tens of microseconds. This timescale is mainly determined by the duration of the received signal segment used for reconstruction, which is ultimately limited by the excitation bandwidth. Therefore, a broader excitation

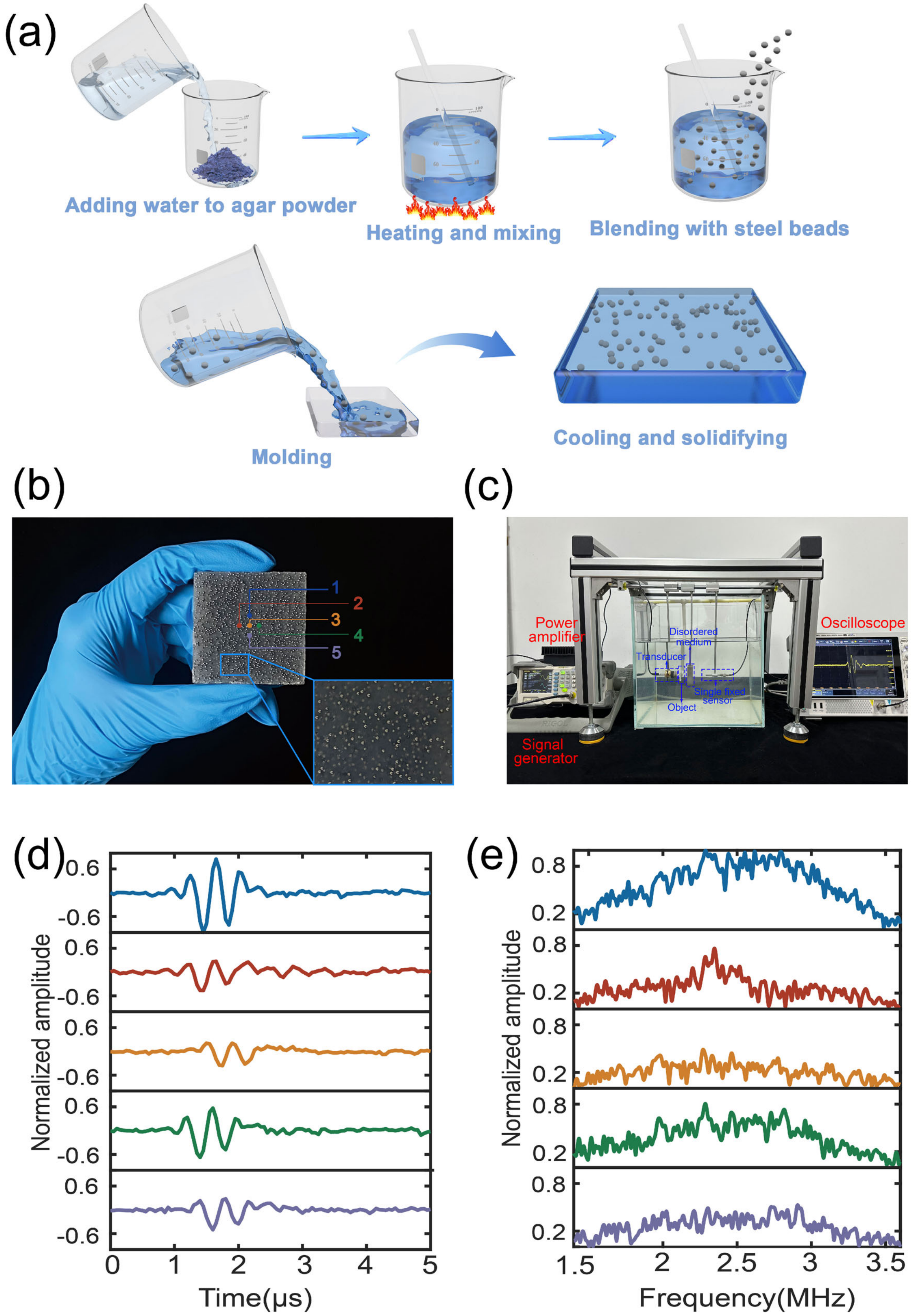

FIGURE 2 | Fabrication and characterization of the disordered medium. (a) Fabrication process of the disordered medium. Photographs of (b) the fabricated disordered medium and (c) the experimental setup. (d) Measured temporal-domain signals and (e) the calculated frequency spectra at 5 particular points behind the medium marked by 5 circular dots in (b).

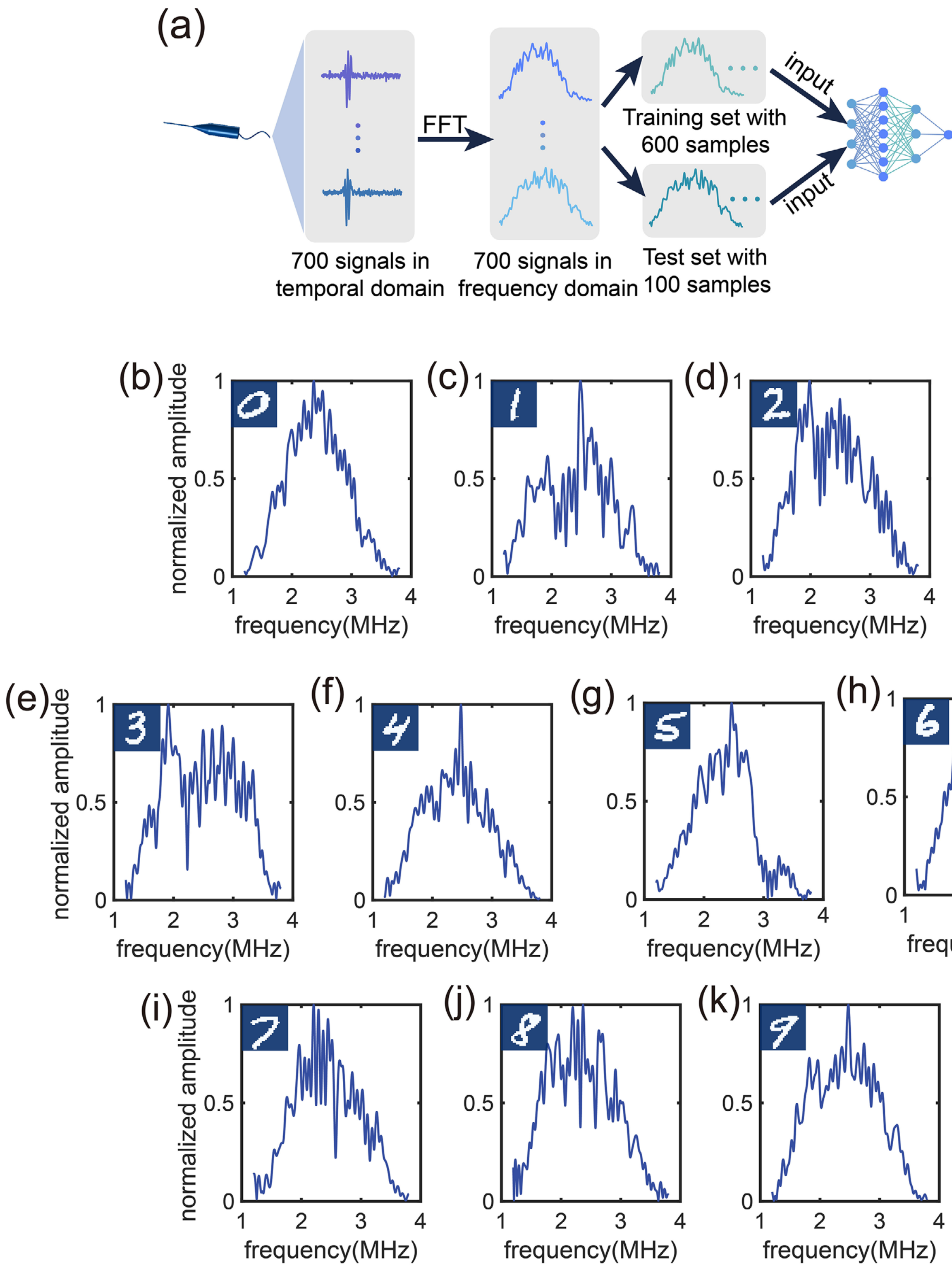

FIGURE 3 | Flow chart of the imaging system and dataset for the neural network training. (a) Process of the dataset preparation, for which 700 recorded signals comprise of different handwritten digits with 600 training sets and 100 test sets. The frequency spectrum of each signal is obtained through the fast Fourier transform and its normalization, which is the input data of the neural network. (b–k) Typical normalized frequency spectra of different handwritten digits' scattering responses received by a single fixed sensor, for 0–9, respectively.

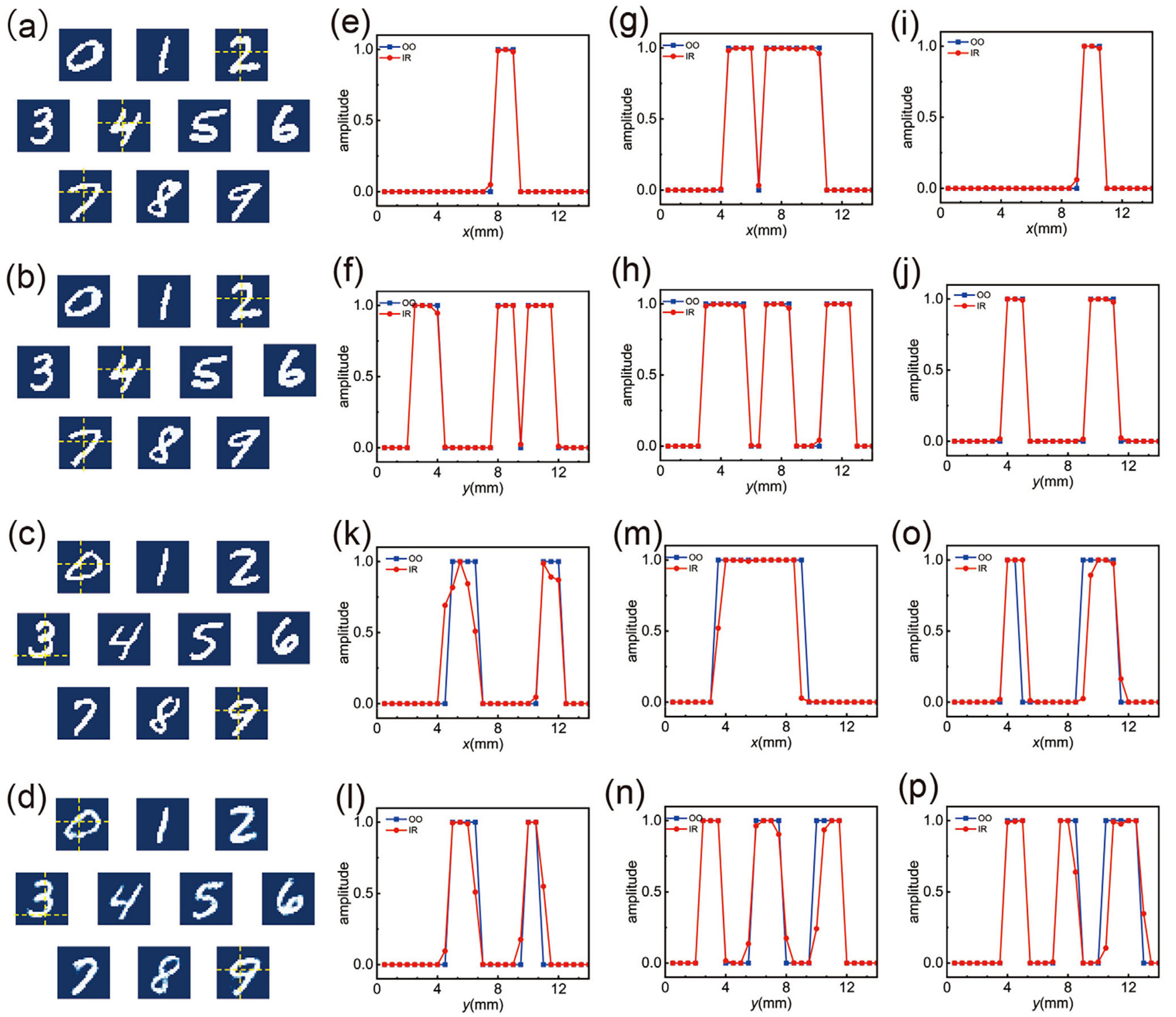

FIGURE 4 | Typical imaging results for both the training and test datasets. (a) Typical original objects of the training set. (b) Corresponding imaging results of objects in (a). (c) Typical original objects of the test set. (d) Corresponding imaging results of objects in (c). (e–j) are the comparisons of original objects and imaging results in (a,b) in terms of profiles of digits 2, 4, and 7 along the horizontal and vertical direction, respectively. (k–p) are the comparison of original objects and imaging results in (c,d) in terms of intensity profiles of digits 0, 3, and 9 along the horizontal and vertical direction, respectively. (OO: original object, IR: imaging result).

bandwidth can further shorten the required signal duration and reduce the overall imaging time. This indicates the potential for real-time imaging of dynamic objects, such as a pulsating heart, which holds significant importance in practical medical applications. The robustness of our mechanism against typical noise is further demonstrated in Section S9.

Figure 5a,b depicts the distribution of SSIM, quantifying the degree of similarity between the imaging results and their corresponding original objects, across each sample in both the training and test sets. In the training set, every sample demonstrates an SSIM exceeding 0.92, with a significant aggregation within the interval of 0.96 to 1.00. In the case of the test set, each sample's imaging results exhibit SSIM surpassing the threshold of 0.6, with no instance falling below this critical mark. It is worth noting, as elucidated in Section S10 and Figure S5, that an SSIM value surpassing 0.6 signifies a commendable reconstruction of the shape information associated with the objects. This indicates the efficacy of our mechanism in achieving precise imaging for all samples, without any instances of poor imaging quality for individual samples. Such consistency and reliability in imaging performance hold crucial significance for practical applications, greatly increasing the detection accuracy. Figure 5c illustrates the training process of the neural network, showing excellent convergence of the model. Although there exists an overfitting issue, it does not affect the effectiveness of our mechanism, and this problem tends to diminish as the sample size of the dataset increases. Furthermore, compared with common object recognition mechanisms based on neural networks [43], which can identify objects but may struggle to reconstruct their precise shape, our method, without any compression of the information utilized for imaging, can reconstruct the geometry of the objects

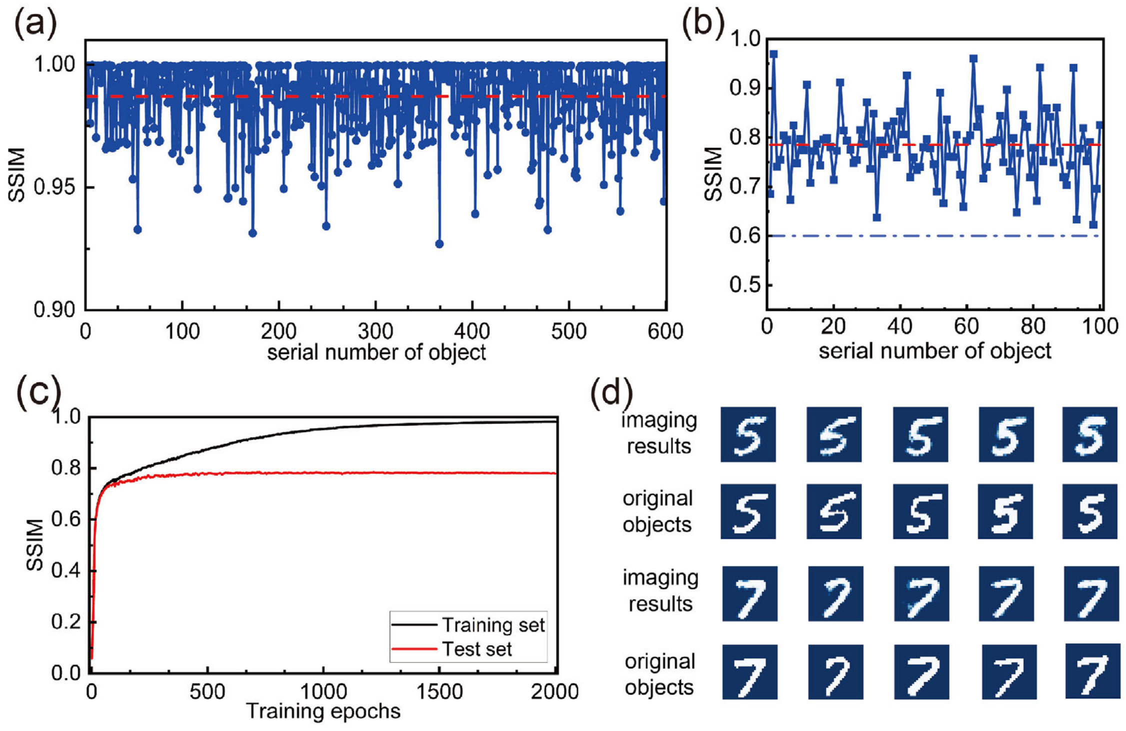

FIGURE 5 | Overall imaging performance demonstration for our single signal imaging system. (a) SSIM distribution of 600 digits in the training set, where the red dashed line represents the average value. (b) SSIM distribution of 100 digits in the test set, where the red dashed line and the baby blue dot dashed line represent the average and threshold value, respectively. (c) Variation curves of SSIM with the training epoch. (d) Imaging results of the same digits of different shapes, accompanied with the original objects in the test set.

that have different shapes but belong to the same number, as shown in Figure 5d. This is mainly because our synthesized frequency-codec mechanism allows the continuous spectrum to serve as the encoding channel with high capacity and independence, such that the full information of the targeted image can be effectively encoded and extracted.

3 | Conclusions

We have demonstrated a mechanism of single-signal acoustic imaging by an AI-assisted synthesized frequency codec that can realize real-time object imaging by a single fixed sensor with the help of a simple disordered medium and AI technology. Using a disordered medium to realize synthesized frequency encoding and a neural network to reconstruct the object's image from spectral "fingerprint", our method can reduce the dimensionality of the imaging system to the greatest extent possible. Unlike most widely explored AI-assisted imaging approaches, where deep learning is typically employed as a post-processing tool applied to data acquired through conventional imaging pipelines, our approach fundamentally reshapes the information acquisition process at the physical level. In our framework, the disordered medium acts as a physics-based encoding layer, while deep learning is subsequently used to decode the encoded information, forming a tightly integrated physical-computational mechanism. Importantly, this framework implies that ultrasonic imaging is no longer fundamentally constrained by the wavelength associated with the center frequency of the probing signal. As long as the spectral response carries sufficient information, subwavelength-scale scatterers can be effectively encoded and retrieved through learning-based decoding, even when long-wavelength acoustic waves are employed. This relaxation of the conventional wavelength constraint is particularly appealing, as it preserves the deep penetration capability of ultrasound while simultaneously enabling enhanced imaging information to be extracted from complex environments. Our findings overcome a long-lasting bottleneck comprising a to-date unresolved compromise between the cost of spatial and temporal dimensions to ensure high image quality at low fabrication and machining costs. In addition, the current scheme already demonstrates a certain degree of generalization capability, as evidenced by its ability to accurately reconstruct previously unseen handwritten digits that were not included in the training set. This indicates that the model captures underlying features rather than merely memorizing the data. Further improvements in generalization can be achieved by expanding the training dataset, incorporating more complex and physically diverse targets, and integrating physics-informed or hybrid learning strategies. Although currently we only demonstrated 2D handwritten digit imaging through the transmission mode of ultrasound wave, our mechanism combining a disordered material with AI is universal and is entirely possible to be extended to complex objects in three-dimensions (3D) using the reflection mode of other wave types. Relying only on randomness and dispersion, a plethora of artificially structured materials and compounds could be employed beyond the medium used in the present experiments. Thus, our approach can provide enough momentum to advance in single-signal-based imaging applications for future low-cost devices, interesting for industrial and medical applications, and beyond.

Author Contributions

B. Liang and W. Wang conceived the idea. W. Wang, B. Liang, and J. Liu performed the theoretical simulations. W. Wang, J. Hu, J. Liu, Y. Tan, C. Zhao, R. Wang, J. Yang and B. Li prepared the samples and performed the experiment. W. Wang, J. Liu, B. Liang, and J. Christensen contributed to the writing of the paper. J. Liu, B. Liang, J. Christensen, and J. Cheng supervised the entire study. All authors contributed to data analyses and discussions.

Acknowledgements

The authors thank Prof. Dazhi Gao at Ocean University of China for fruitful discussions and for his contribution in the initial stage of the experiment. This work was supported by the Fundamental and Interdisciplinary Disciplines Breakthrough Plan of the Ministry of Education of China (Grant No. JYB2025XDXM805 to B. Liang), the National Key Research and Development Program of China (Grant Number 2022YFA1404402 to B. Liang), the National Natural Science Foundation of China (Grant Nos. 12304493 to J. Liu, 12174190 to J. Yang), the Natural Science Foundation of Jiangsu Province (Grant Nos. BK20233001 to B. Liang, BK20230767 to J. Liu), the Fundamental Research Funds for the Central Universities (Grant No. KG202501 to J. Liu), the China Postdoctoral Science Foundation (Grant No. 2025M771844 to B. Li), High-Performance Computing Center of Collaborative Innovation Center of Advanced Microstructures and a project funded by the Priority Academic Program Development of Jiangsu Higher Education Institutions. J. Christensen acknowledges support from the Spanish Ministry of Science and Innovation through a Consolidación Investigadora grant (CNS2022-135706).

Conflicts of Interest

The authors declare no conflicts of interest.

Data Availability Statement

The data that support the findings of this study are available from the corresponding author upon reasonable request.

References

1. H. J. Hu, H. Huang, M. H. Li, et al., "A Wearable Cardiac Ultrasound Imager," *Nature* 613 (2023): 667–675, https://doi.org/10.1038/s41586-022-05498-z.

2. B. W. Drinkwater and P. D. Wilcox, "Ultrasonic Arrays for Non-Destructive Evaluation: a Review," *NDT & E International* 39 (2006): 525–541, https://doi.org/10.1016/j.ndteint.2006.03.006.

3. M. V. Felice, A. Velichko, and P. D. Wilcox, "Accurate Depth Measurement of Small Surface-Breaking Cracks Using an Ultrasonic Array Post-Processing Technique," *NDT & E International* 68 (2014): 105–112, https://doi.org/10.1016/j.ndteint.2014.08.004.

4. C. H. Wang, X. Y. Chen, L. Wang, et al., "Bioadhesive Ultrasound for Long-Term Continuous Imaging of Diverse Organs," *Science* 377 (2022): 517–523, https://doi.org/10.1126/science.abo2542.

5. H. G. Yun, R. Rayhana, S. Pant, M. Genest, and Z. Liu, "Nonlinear Ultrasonic Testing and Data Analytics for Damage Characterization: a Review," *Measurement* 186 (2021): 110155, https://doi.org/10.1016/j.measurement.2021.110155.

6. S. Singh and A. Goyal, "The Origin of Echocardiography: a Tribute to Inge Edler," *Texas Heart Institute Journal* 34 (2007): 431.

7. H. C. Tang, Y. Y. Yang, Z. Liu, et al., "Injectable Ultrasonic Sensor for Wireless Monitoring Intracranial Signals," *Nature* 630 (2024): 84–90.

8. J. L. Sutton, "Underwater Acoustic Imaging," *Proceedings of the IEEE* 67 (1979): 554–566, https://doi.org/10.1109/PROC.1979.11283.

9. Z. B. Lin, J. Z. Liu, Y. Hu, et al., "Echo-Vision: a Dual-Function Ultrasonic Platform for Acoustic Energy Harvesting and Varifocal Echo Imaging," *Advanced Energy Materials* 16 (2026): 06618.

10. Z. L. Li, L. X. Huang, Q. L. Sun, et al., "3D Acoustic Imaging Hitting the Diffraction Limit via Fully Parameter-Optimized Meta-Lens and Frequency-Domain Reconstruction," *Advanced Materials* 37 (2025): 08453.

11. L. S. Zeng, Z. B. Lin, Z. L. Li, et al., "High-Resolution Manifold Acoustic Holography Based on High-Pixel-Array Binary Metasurfaces," *Advanced Materials* 37 (2025): 2420229.

12. K. K. Shung and M. Zipparo, "Ultrasonic Transducers and Arrays," *IEEE Engineering in Medicine and Biology Magazine* 15 (1996): 20–30, https://doi.org/10.1109/51.544509.

13. A. Macovski, "Ultrasonic Imaging Using Arrays," *Proceedings of the IEEE* 67 (1979): 484–495.

14. M. Krause, F. Mielentz, B. Milman, W. Muller, V. Schmitz, and H. Wiggenhauser, "Ultrasonic Imaging of Concrete Members Using an Array System," *NDT & E International* 34 (2001): 403–408, https://doi.org/10.1016/S0963-8695(01)00007-X.

15. J. Rao, M. Ratassepp, and Z. Fan, "Guided Wave Tomography Based on Full Waveform Inversion," *IEEE Transactions on Ultrasonics, Ferroelectrics, and Frequency Control* 63 (2016): 737–745.

16. X. D. Yu, M. Ratassepp, and Z. Fan, "Damage Detection in Quasi-Isotropic Composite Bends Using Ultrasonic Feature Guided Waves," *Composites Science and Technology* 141 (2017): 120–129, https://doi.org/10.1016/j.compscitech.2017.01.011.

17. K. K. Shung, "High Frequency Ultrasonic Imaging," *Journal of Medical Ultrasound* 17 (2009): 25–30, https://doi.org/10.1016/S0929-6441(09)60012-6.

18. P. Kruizinga, P. van der Meulen, A. Fedjajevs, et al., "Compressive 3D Ultrasound Imaging Using a Single Sensor," *Science Advances* 3 (2017): 1701423, https://doi.org/10.1126/sciadv.1701423.

19. P. van der Meulen, P. Kruizinga, J. G. Bosch, and G. Leus, "Computational Ultrasound Carotid Artery Imaging with a Few Transceivers: an Emulation Study," *IEEE Transactions on Ultrasonics, Ferroelectrics, and Frequency Control* 6 (2020): 721–731.

20. M. P. Edgar, G. M. Gibson, and M. J. Padgett, "Principles and Prospects for Single-Pixel Imaging," *Nature Photonics* 13 (2019): 13–20, https://doi.org/10.1038/s41566-018-0300-7.

21. G. M. Gibson, S. D. Johnson, and M. J. Padgett, "Single-Pixel Imaging 12 Years On: a Review," *Optics Express* 28 (2020): 28190, https://doi.org/10.1364/OE.403195.

22. S. Yan, Y. W. Sun, N. Fengchao, Z. W. Liu, H. G. Liu, and X. F. Chen, "Image Reconstruction through a Nonlinear Scattering Medium via Deep Learning," *Photonics Research* 12 (2024): 2047, https://doi.org/10.1364/PRJ.523728.

23. X. T. Lai, Q. Y. Li, Z. Y. Chen, X. P. Shao, and J. X. Pu, "Reconstructing Images of Two Adjacent Objects Passing through Scattering Medium via Deep Learning," *Optics Express* 29 (2021): 43280, https://doi.org/10.1364/OE.446630.

24. B. Assouar, B. Liang, Y. Wu, Y. Li, J. C. Cheng, and Y. Jing, "Acoustic Metasurfaces," *Nature Reviews Materials* 3 (2018): 460–472, https://doi.org/10.1038/s41578-018-0061-4.

25. T. Brunet, J. Leng, and O. Mondain-Monval, "Soft Acoustic Metamaterials," *Science* 342 (2013): 323–324, https://doi.org/10.1126/science.1241727.

26. T. Brunet, A. Merlin, B. Mascaro, et al., "Soft 3D Acoustic Metamaterial with Negative Index," *Nature Materials* 14 (2015): 384–388, https://doi.org/10.1038/nmat4164.

27. G. C. Ma, M. Yang, S. W. Xiao, Z. Y. Yang, and P. Sheng, "Acoustic Metasurface with Hybrid Resonances," *Nature Materials* 13 (2014): 873–878, https://doi.org/10.1038/nmat3994.

28. S. A. Cummer, J. Christensen, and A. Alu, “Controlling Sound with Acoustic Metamaterials,” *Nature Reviews Materials* 1 (2016): 16001, https://doi.org/10.1038/natrevmats.2016.1.

29. N. M. Estakhri, B. Edwards, and N. Engheta, “Inverse-Designed Metastructures That Solve Equations,” *Science* 363 (2019): 1333–1338, https://doi.org/10.1126/science.aaw2498.

30. O. I. Abiodun, A. Jantan, A. E. Omolara, K. V. Dada, N. A. Mohamed, and H. Arshad, “State-of-the-Art in Artificial Neural Network Applications: a Survey,” *Heliyon* 4 (2018): 00938.

31. A. K. Jain, J. C. Mao, and K. M. Mohiuddin, “Artificial Neural Networks: a Tutorial,” *Computer* 29 (1996): 31–44, https://doi.org/10.1109/2.485891.

32. Y. LeCun, Y. Bengio, and G. Hinton, “Deep Learning,” *Nature* 521 (2015): 436–444, https://doi.org/10.1038/nature14539.

33. X. Lin, Y. Rivenson, N. T. Yardimei, et al., “All-Optical Machine Learning Using Diffractive Deep Neural Networks,” *Science* 361 (2018): 1004–1008, https://doi.org/10.1126/science.aat8084.

34. M. Horodynski, M. Kuhmayer, C. Ferise, S. Rotter, and M. Davy, “Anti-Reflection Structure for Perfect Transmission through Complex media,” *Nature* 607 (2022): 281–286, https://doi.org/10.1038/s41586-022-04843-6.

35. M. Horodynski, M. Kühmayer, A. Brandstötter, et al., “Optimal Wave Fields for Micromanipulation in Complex Scattering Environments,” *Nature Photonics* 14 (2020): 149–153, https://doi.org/10.1038/s41566-019-0550-z.

36. F. Riboli, N. Caselli, S. Vignolini, et al., “Engineering of Light Confinement in Strongly Scattering Disordered media,” *Nature Materials* 13 (2014): 720–725, https://doi.org/10.1038/nmat3966.

37. R. McIntosh, A. Goetschy, N. Bender, et al., “Delivering Broadband Light Deep inside Diffusive media,” *Nature Photonics* 18 (2024): 744–750.

38. H. Cao, A. P. Mosk, and S. Rotter, “Shaping the Propagation of Light in Complex media,” *Nature Physics* 18 (2022): 994–1007, https://doi.org/10.1038/s41567-022-01677-x.

39. N. Bender, A. Yamilov, A. Goetschy, H. Yilmaz, C. W. Hsu, and H. Cao, “Depth-Targeted Energy Delivery Deep inside Scattering media,” *Nature Physics* 18 (2022): 309–315, https://doi.org/10.1038/s41567-021-01475-x.

40. M. Egmont-Petersen, D. de Ridder, and H. Handels, “Image Processing with Neural Networks—A Review,” *Pattern Recognition* 35 (2002): 2279–2301, https://doi.org/10.1016/S0031-3203(01)00178-9.

41. Y. B. Xie, T. H. Tsai, A. Konneker, B. I. Popa, D. J. Brady, and S. A. Cummer, “Single-Sensor Multispeaker Listening with Acoustic Metamaterials,” *Proceedings of the National Academy of Sciences USA* 112 (2015): 10595–10598, https://doi.org/10.1073/pnas.1502276112.

42. Y. LeCun, C. Cortes, and C. J. Borges, The MNIST database of handwritten digits (1998) http://yann.lecun.com/exdb/mnist.

43. J. X. Li, D. Mengu, N. T. Yardimci, et al., “Spectrally Encoded Single-Pixel Machine Vision Using Diffractive Networks,” *Science Advances* 7 (2021): abd7690, https://doi.org/10.1126/sciadv.abd7690.

Supporting Information

Additional supporting information can be found online in the Supporting Information section.

Supporting File: adfm76440-sup-0001-SuppMat.docx.